Materials Research Bulletin 188 (2025) 113397

Contents lists available at ScienceDirect

Materials Research Bulletin

journal homepage: www.elsevier.com/locate/matresbu

Research Papers

Luminescent sensing of Hg^{2+} ions using MOF-808 combined with Au_{25}@BSA nanoclusters

L.G. Barbata [a], M. Mazaj [b], R. Ettlinger [c], G. Ficarra [a], P. Castronovo [a], A. Sciortino [a], F. Messina [a], R.E. Morris [d], G. Buscarino [a,*]

[a] Dipartimento di Fisica e Chimica - Emilio Segrè, Università di Palermo, Via Archirafi, 36, I-90123 Palermo, Italy
[b] National Institute of Chemistry, Hajdrihova 19, 1000 Ljubljana, Slovenia
[c] TUM School of Natural Sciences, Technical University of Munich Lichtenbergstr.4, 85748 Garching b. München, Germany
[d] EastChem School of Chemistry, University of St Andrews, North Haugh, St Andrews, UK

ARTICLE INFO

Keywords:
LMOFs
AuNCs
Luminescent sensors
Heavy metals

ABSTRACT

The detection of Hg^{2+} ions in aqueous environments is crucial due to their environmental toxicity and potential health risks. In this study, we present a novel luminescent sensor based on Metal-Organic Framework MOF-808 functionalized with Au_{25}@BSA gold nanoclusters (AuNCs) for the highly sensitive detection of trace Hg^{2+} ions. MOF-808, known for its robust structure and versatile chemical environment, provides an ideal platform for incorporating gold nanoclusters that exhibit unique optical properties. The integration of Au_{25}@BSA in MOF-808 framework enhances the temporal and thermal stability of the gold nanoclusters while preserving their photoluminescence properties. The MOF-808/Au_{25}@BSA composite behaves as a sensor relying on the quenching effect of Hg^{2+} on the luminescence of the gold nanoclusters embedded within the MOF matrix, offering a highly selective and sensitive detection method at concentrations as low as nM levels. Comprehensive characterizations of the MOF-808/Au_{25}@BSA composite were conducted. This sensor demonstrates remarkable performance with high sensitivity, selectivity, and stability, making it a promising tool for environmental monitoring and analysis. This work highlights the potential of MOF-based luminescent sensors combined with gold nanoclusters in advancing the field of sensing applications.

1. Introduction

Metal-organic frameworks (MOFs) are hybrid materials formed by the coordination of metal ions or (oxo)clusters with organic linkers, resulting in highly porous and crystalline structures [1,2]. Owing to their tunable pore size, large surface area, and versatility in functionalization, MOFs have been extensively studied for applications ranging from gas storage and separation [3,4] to carbon capture [5,6], catalysis [7,8] and drug delivery [9,10]. In recent years, there has been growing interest in employing MOFs for chemical sensing, particularly in the detection of hazardous ions such as heavy metals [11]. The inherent porosity and stability of MOFs provide excellent platforms for developing sensors that exhibit high sensitivity and selectivity. Luminescent MOFs (LMOFs) are a particularly promising subclass of MOFs displaying functional photophysical properties that can be used in many applications like LEDs, bioimaging, anti-counterfeiting, solar cells, and optical sensing. Their ability to host luminescent species—either within the framework or in the pores—makes them ideal for fluorescence-based sensing. The combination of high surface area and the potential for metal–ligand interactions allow these materials to interact with analytes in a highly controlled manner, often leading to changes in luminescence that can be detected and quantified [12–15].

Today, one of the most critical challenges in environmental sensing is the detection of toxic heavy metals such as mercury (Hg^{2+}), which is highly harmful to human health even at trace levels [16]. The development of luminescent sensors capable of detecting Hg^{2+} with high sensitivity and selectivity in aqueous environments has become an important research focus [17,18]. MOFs provide an ideal scaffold for this purpose due to their structural tunability, which allows precise control over pore size and functionalization, enabling the selective capture of specific ions based on size exclusion and chemical interactions [19,20]. Several MOFs have been explored as luminescent sensors for Hg^{2+}. For example, Zhang et al. [21] have reported that NH_2_MIL-53(Al) could be used as sensor for aqueous Hg^{2+} with a limit

* Corresponding author.
E-mail address: gianpiero.buscarino@unipa.it (G. Buscarino).

https://doi.org/10.1016/j.materresbull.2025.113397
Received 30 October 2024; Received in revised form 18 February 2025; Accepted 21 February 2025
Available online 22 February 2025

of detection (LOD) of 0.15 μM and a very good selectivity respect to other common metal ions. Moreover Guo et al. [22] have synthesized Eu-Ca-MOF which works as ratiometric sensor for Hg^{2+} ions in trace concentrations (LOD= 2.6 nM) with an extreme selectivity to all common M^{2+} and M^{3+} ions in aqueous solution. Despite the numerous works on sensors based on LMOFs, combining luminescent atomically precise gold nanoclusters with MOFs is still an underexplored opportunity. Gold nanoclusters (AuNCs) are known for their strong luminescence and unique size-dependent optical properties, which have been harnessed for various sensing applications [23,24]. In particular Au_{25} clusters capped by Bovine serum albumin (Au_{25}@BSA), has been demonstrated to exhibit remarkable chemical stability and fluorescence [25]. Further, Xie et al. reported that Au@$_{25}$BSA is a sensitive and selective sensor for Hg^{2+} ions in trace level concentrations [26]. However, AuNCs tend to be unstable at room temperature and typically require storage at low temperatures (4 °C) to maintain their luminescent properties [27]. Interestingly, these clusters are usually no larger than 2 nm, which is comparable to the size of many MOFs cages. This allows in principle to incorporate AuNCs in MOFs, which may enhance their room-temperature stability and pave the way to interesting applications founded on the synergy between the optical response of AuNCs and the chemical properties of the MOFs.

In this study, we synthesized MOF-808, a zirconium-based MOF with a robust structure and high surface area, [28,29] and combined it with Au_{25}@BSA nanoclusters to create a highly sensitive and stable luminescent sensor for detecting trace concentrations of Hg^{2+} ions in aqueous solutions. The obtained MOF-808/Au_{25}@BSA composite was structurally and optically characterized by powder X-ray diffraction (PXRD), N_2 gas sorption analysis, FTIR spectroscopy, UV/Vis absorption spectroscopy, time resolved photoluminescence (TRPL), and its sensing performance was evaluated through steady state photoluminescence. The integration of gold nanoclusters into the MOF-808 framework enhances their stability at room temperature, eliminating the need for cold storage, while guaranteeing high selectivity and sensitivity for Hg^{2+} detection in the nanomolar range. This work demonstrates the potential of combining MOFs with gold nanoclusters to create a new family of functional nanocomposites that can be used as robust, highly sensitive and selective sensors for environmental monitoring.

2. Materials and methods

2.1. Chemicals

Zirconium chloride ($ZrCl_4$, 99.8 %, Alfa-Aesar ≥99.5 %), 1,3,5-Benzenetricarboxylic acid (H_3BTC, 98 %,Fisher Scientific), Isopropyl alcohol (≥99 %, Sigma-Aldrich,) Formic acid (≥96 %, Sigma-Aldrich), Acetic acid (≥99 % Sigma-Aldrich), Ethanol absolute (≥99 % VWR), Tetrachloroauric(III) acid trihydrate ($HAuCl_4{\cdot}3H_2O$, 99 % Sigma-Aldrich), Sodium hydroxide (NaOH, ≥99 % Sigma-Aldrich), Bovine serum albumin (≥98 % Sigma-Aldrich), Hydrochloric acid (37 % Sigma-Aldrich), Nitric Acid (65 %, Sigma-Aldrich), Phosphate buffer solution pH=7 (Sigma-Aldrich), Ethylenediaminetetraacetic acid (EDTA, 98 % Aldrich), Mercury nitrate monohydrate ($Hg(NO_3)_2{\cdot}H_2O$), and other metal ions were all analysis reagent grade and purchased from Sigma-Aldrich. Milli-Q water (18.2 MΩ cm^{-1}) was used throughout the experiments.

2.2. Synthesis

2.2.1. Synthesis and purification of Au_{25}@BSA

Au_{25}@BSA nanoclusters were synthesized following the protocol reported by Xie et al. [25], with slight modifications. Prior to the synthesis, all glassware was rigorously cleaned with Aqua Regia (3:1 mixture of HCl and HNO_3) and thoroughly rinsed with ultrapure water to eliminate any metal contaminants. An aqueous solution of $HAuCl_4$ (10 mM) was prepared by dissolving the salt in 5 mL of ultrapure water. Separately, a Bovine Serum Albumin (BSA) solution (50 mg/mL) was prepared by dissolving the protein in 5 mL of ultrapure water. Both solutions were heated until they reached 37 °C. Subsequently, the BSA solution was placed in an oil bath maintained at 37 °C, and the $HAuCl_4$ solution was added to it under vigorous stirring. After 2 mins, NaOH solution (0.5 mL, 1 M) was added to adjust the pH to 11. The reaction mixture was maintained at 37 °C in the oil bath under continuous stirring for 12 h. At the end of the reaction, a red-brown solution was obtained (Fig. S1).

The as-synthesized Au_{25}@BSA solution was purified to remove unreacted BSA and other byproducts according to the method described by Guan et al. [30]. Briefly, 2 mL of the Au_{25}@BSA solution was added into a glass vial, followed by rapid injection of 2 mL of Zn^{2+} solution (10 mM). The resulting precipitate was centrifuged at 6000 rpm for 10 mins and washed three times with distilled water. After discarding the supernatant, the precipitate was redispersed in 2 mL of PBS solution, yielding a clear brown solution. This was further diluted to a final volume of 20 mL with ultrapure water.

2.2.2. Synthesis of MOF-808

MOF-808 was synthesized following a room temperature approach reported by Dai et al. [29], which involves the initial preparation of Zr_6-oxoclusters as metal nodes of the MOF. In the first step, Zr_6-oxoclusters were synthesized by dissolving $ZrCl_4$ (10 g) in a mixture of acetic acid (15 mL) and isopropanol (25 mL). The mixture was stirred at 500 rpm and heated to 120 °C for 60 mins under reflux. The resulting product was collected by gravity filtration, washed with cold isopropanol, and dried in air at room temperature. Next, Zr_6-oxoclusters (1.2 g) were dissolved in formic acid (3 mL) under stirring at 600 rpm. Subsequently, H_2O (5 mL) was added dropwise, and the mixture was stirred until it became completely colourless. Then, 1,3,5-benzenetricarboxylic acid (300 mg) was added, and the reaction mixture was stirred overnight at room temperature. The solid product was collected by centrifugation at 14,500 rpm for 5 mins, followed by washing with 40 mL of H_2O and 40 mL of ethanol. The washed solid was dried at 60 °C in air and activated under vacuum at 120 °C overnight to yield the final MOF-808 product.

2.2.3. MOF-808/Au_{25}@BSA preparation

MOF-808 powders (100 mg) were dispersed in 20 mL of the diluted, purified Au_{25}@BSA solution and sonicated for 10 mins. The resulting dispersion was then stirred continuously for 24 h. The product was subsequently recovered by centrifugation at 12,000 rpm for 10 mins, washed three times with 50 mL of ultrapure water to remove unbound clusters, and dried at 50 °C overnight.

2.3. Characterization and instrumentations

PXRD measurements were performed with a Malvern PANalytical Empyrean Alpha 1 machine in Bragg-Brentano geometry using Cu Kα1 radiation in the range from 3° to 70°. FTIR spectroscopy was carried out using a Shimadzu IR Affinity-1 FTIR spectrophotometer in transmittance mode from 400 to 4000 cm^{-1}. BET-specific surface area determination from N_2 isotherms (77 K) was carried out according to the BET theory [31,32]. Data was recorded on an Anton Paar Autosorb IQ3 High Vacuum Physisorption Analyzer. The sample (~50 mg) was added to a frit tube and activated in vacuum (150 °C or 400 °C, ~3×10^{-5} mbar, 12 h) prior to the measurement. Thermogravimetric measurements were performed using a Q5000 IR apparatus (TA Instruments) under an inert nitrogen atmosphere. The analysis was conducted over a temperature range of 25 to 700 °C at a scanning rate of 20 °C/min. The XRF spectra were recorded using a Bruker Tracer III–SD Series AXS portable spectrometer having a Rhodium tube as X-ray generator and a silicon drift XFlash® with Peltier cooling system as a detector. The spectra were acquired with a voltage of 40 Kv and a current of 11 μA. In all spectra, there are also signals of Ar, Ni, Fe, Pt and Rh due respectively to the

atmosphere and to the instrumental components. Data analysis was performed using the ARTAX® software.

The absorption spectra were acquired by using a single-beam optical fiber spectrophotometer setup with Avantes AvaLight-DH-S-BAL dual halogen-deuterium light source and a Avantes AvaSpec-ULS2048CL-EVO-RS spectrometer allowing the investigation of a spectral window between 200 and 800 nm.

Time-resolved photoluminescence (TRPL) measurements were performed with OPOTEK VIBRANT tunable laser (pulse length of 5 ns, repetition rate 10 Hz) coupled with a Princeton Instruments Acton SP2300i spectrograph with PI-MAX CCD detector. All the TRPL measurements were acquired at a fixed excitation wavelength of 405 nm (bandwidth=4 nm), with a grating having λ_{blaze}=300 nm and 150 groves/mm and slit aperture of 200 μm. The lifetimes curves were fitted with a double exponential decay function (Eqs. S1). The steady state fluorescence measurements were performed with a 405 nm Thorlabs CPS405 laser diode as excitation source and with a spectrophotometer setup composed by an Acton SpectraPro 2300i monochromator and a Princeton Instruments Pixis 400 CCD camera as detector, a 475 nm long pass filter was used to block stray light and diffuse excitation radiation. Measurements on the stability of MOF-808@Au_{25}@BSA steady state luminescence were conducted on the same sample in powders put between microscope glass slides, stored at room temperature and monitored one time per month. All sensing tests were conducted with 1 mm quartz cuvette. Fluorescence titration of MOF-808/Au_{25}@BSA with Hg^{2+} and selectivity test with metal ions were conducted dispersing by sonication MOF-808/Au_{25}@BSA powders in water with a concentration of 500 μg/mL and with the use of EDTA (0.5 mM) as masking agent for Cu^{2+} ions as previously reported by different works [33–35].

3. Results and discussions

3.1. Structural characterization

We first investigated the crystallinity of MOF-808 obtained by room temperature synthesis and the stability of the framework after the loading with Au_{25}@BSA. Fig. 1 reports the PXRD patterns of MOF-808 and MOF-808/Au_{25}@BSA. Regarding MOF-808, the XRD pattern clearly shows that the MOF powders are highly crystalline with very sharp peaks at 4.3°, 8.2°, 8.6°, 9.9° and 10.8° (Miller indices 111, 311, 222, 400, 331 respectively), which undoubtedly match the known MOF-808 structure, as previously reported in the literature [28,29]. Meanwhile, data collected for MOF-808/Au_{25}@BSA confirm the retention of the main diffraction peaks, indicating that the incorporation of Au_{25}@BSA nanoclusters does not significantly alter the crystal structure of MOF-808. Minor shifts in peak positions and variations in intensity suggest possible interactions between the MOF framework and the gold nanoclusters. No new peaks are visible indicating that gold nanoclusters are homogeneously distributed on or inside MOF particles without forming separate crystalline phases.

To further investigate the chemical structure and confirm the successful coupling of Au_{25}@BSA nanoclusters with MOF-808, FTIR-ATR spectroscopy was performed (Fig. 2). MOF-808 infrared spectra show several characteristics sharp peaks. According to the literature the peak, at 1610 cm^{-1} is related to the stretching of aromatic C = C bonds belonging to the benzene tri-carboxylate (BTC) linker, the peaks at 1560, 1441 1385 cm^{-1} are related to the symmetrical and asymmetrical stretching of the carboxylate groups, while the peak at 657 cm^{-1} is related to the collective vibrations of the Zr_6-oxoclusters node within MOF-808 involving multiple Zr–O bonds [36]. Examining the spectra of MOF-808/Au_{25}@BSA confirms the presence all aforementioned vibrations of the framework, supporting the XRD data in the assumption that MOF-808 withstood combination with Au_{25}@BSA. Moreover, the broad band between 3400 and 3200 cm^{-1} highlights the presence of -OH and -NH_2 groups, while the increase in relative intensity of the bands at 1610 and 1560 cm^{-1} can be attributed to the overlapping of these bands with the amide I and amine scissoring bands of BSA [37]. Therefore, also the FTIR spectra of MOF-808/Au_{25}@BSA confirm the efficient combination of gold clusters with the MOF framework.

To complement the structural characterization of the materials, we also conducted N_2 adsorption measurements, and the Brunauer-Emmett-Teller (BET) surface area was calculated (Fig. S2). MOF-808 exhibits a type I isotherm, with a specific surface area of ≈ 2090 m^2 g^{-1}, which is consistent with the values reported in the literature [28,29]. Conversely, the MOF-808/Au_{25}@BSA composite shows a significantly lower BET surface area of 465 m^2 g^{-1}. This reduction can be attributed to Au_{25}@BSA nanoclusters, which increase the mass and thus reducing the surface area per unit mass. Additionally, the nanoclusters may partially limit the accessibility of N_2 molecules to the internal surface of MOF-808. The decrease in surface area suggests successful combination of the nanoclusters with the framework, impacting the overall porosity. We performed thermogravimetric analysis (TGA) and differential thermal analysis (DTA) on both MOF-808 and MOF-808/Au_{25}@BSA. The corresponding results are shown in Fig. 3.

The TGA curve for MOF-808 (Fig. 3a) reveals three distinct weight

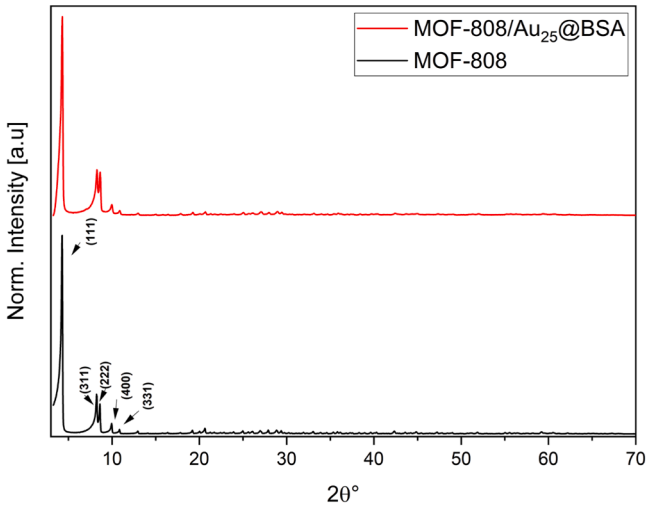

Fig. 1. X-ray diffraction (XRD) patterns of MOF-808 (black) and the MOF-808/Au_{25}@BSA composite (red). The labels indicate the Miller indices of the observed peaks.

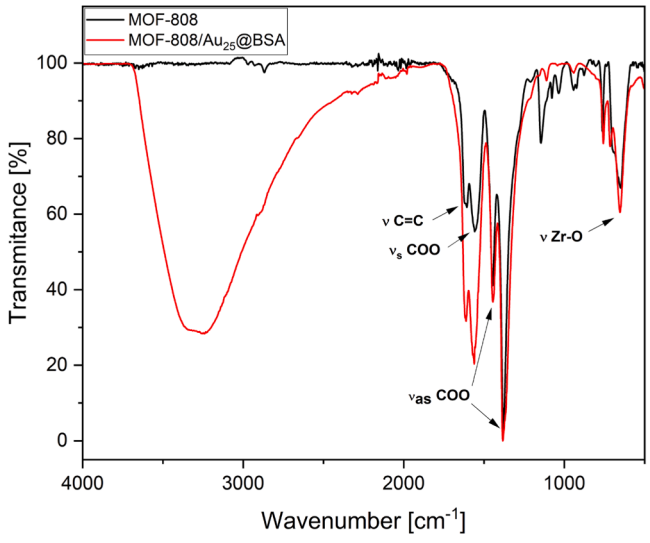

Fig. 2. FTIR-ATR spectra of MOF-808 (black) and the MOF-808/Au_{25}@BSA composite (red). Labels indicate the attribution of the main observed spectral features to characteristic vibrational modes of the system.

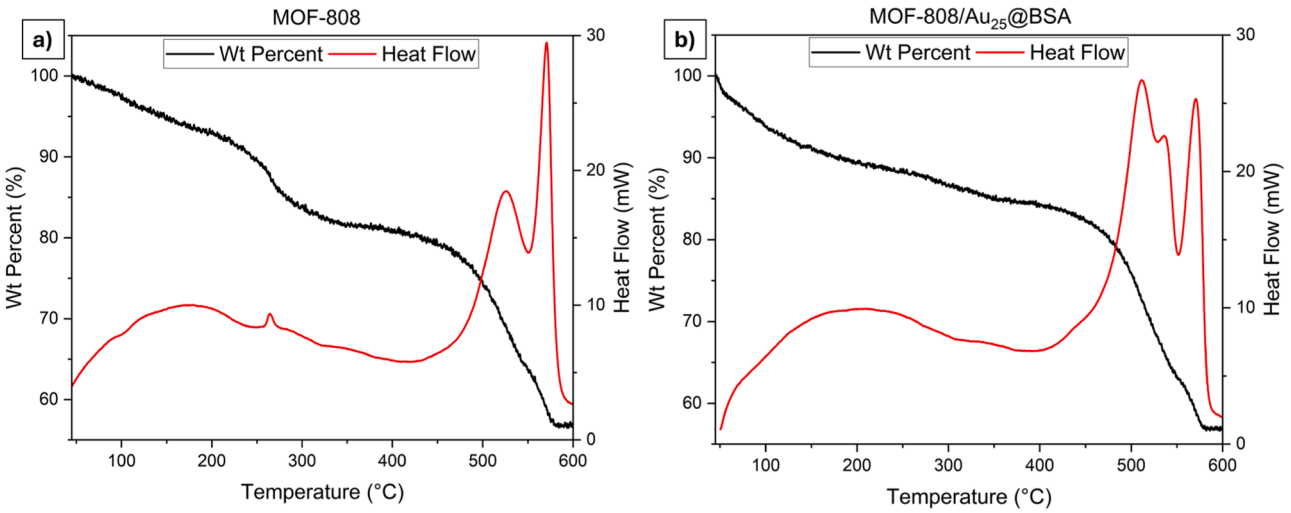

Fig. 3. TGA/DTA analysis of MOF-808 (a) and MOF-808/Au_{25}@BSA (b). The black curve represents the thermogravimetric weight loss (TGA), while the red curve corresponds to the differential thermal analysis (DTA) indicating heat flow.

loss steps. The first minor weight loss below 200 °C is attributed to the desorption of water and ethanol molecules. The second step, occurring between 200 °C and 350 °C, corresponds to the decomposition of formic acid molecules coordinated with the Zr_6 nodes. A major weight loss is observed between 400 °C and 600 °C, which is attributed to the combustion of the BTC linker coordinated with the Zr_6 nodes. According to the DTA, this combustion occurs at 520 °C. Following this, BTC is expected to completely burn out, and the Zr_6 oxoclusters decompose at 570 °C, leaving zirconium dioxide (ZrO_2) as the final residue [38]. The TGA/DTA analysis of MOF-808/Au_{25}@BSA (Fig. 3b) exhibits a similar profile to that of MOF-808 but with some notable differences. The initial weight loss below 200 °C is slightly higher than that to MOF-808, likely due to the increased adsorption of water caused by the hydrophilic BSA coating on the Au_{25}@BSA clusters. The weight loss between 200 °C and 350 °C is less pronounced, suggesting that BSA may coordinate with the accessible binding sites of MOF-808, replacing the formic acid. Meanwhile the weight loss between 400 °C and 600 °C is greater than MOF-808, due to the decomposition of both the BTC linker and the organic BSA coating of the Au_{25} nanoclusters. Notably, the DTA of MOF-808/Au_{25}@BSA shows an additional peak at 535 °C, likely corresponding to the decomposition of the BSA. Finally, the residual weight at the end of the analysis (approximately 2 % for MOF-808/Au_{25}@BSA) is slightly higher than that of MOF-808. This increased residue confirms the presence of thermally stable metallic gold in the sample.

Finally, we conducted XRF analysis on both MOF-808 and MOF-808/Au_{25}@BSA to confirm the presence of gold in the composite material and the spectra are reported in Fig. 4.

The XRF spectrum of pristine MOF-808 clearly shows the characteristic zirconium peaks, specifically the Kα₁ and Kβ₁ lines at 15.76 and 17.68 keV, respectively, along with the Lα₁ line at 2.04 keV. In contrast, the XRF spectrum of the MOF-808/Au_{25}@BSA composite displays, in addition to the Zr lines, two distinct gold peaks: the Au Lα and Lβ lines at approximately 9.7 and 11.5 keV, respectively [39]. These findings provide definitive confirmation of the successful incorporation of Au_{25}@BSA nanoclusters into the composite material.

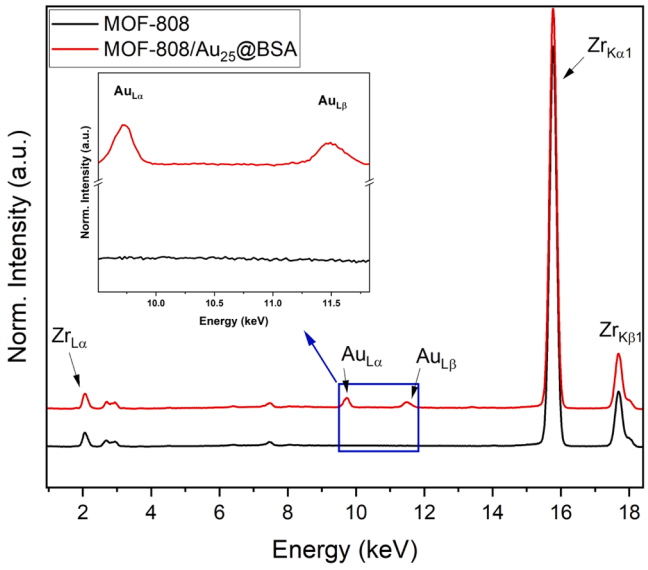

Fig. 4. XRF spectra of MOF-808 (black) and MOF-808/Au_{25}@BSA composite (red). The labelled peaks indicate the XRF lines of zirconium (Zr) and gold (Au). The inset highlights an enlarged region of the spectrum to better visualize the Au lines.

3.2. Optical characterization

We next investigated the luminescent properties of both Au_{25}@BSA clusters and MOF-808/Au_{25}@BSA. As reference we first characterized Au_{25}@BSA. In Fig. 5 absorption and steady state emission spectra of Au_{25}@BSA clusters are reported.

Absorption spectra (Fig. 5a) show an evident band at 275 nm which is due to the absorbance of aromatic amino acids, mainly tryptophan and tyrosine present in BSA. At longer wavelengths, the absorption spectrum appears largely unstructured, suggesting large scattering contributions mostly concealing the absorption bands in the 300 - 450 nm region due to HOMO–LUMO electronic transitions within Au clusters, as previously reported by many different works [25,37,40]. Meanwhile steady state emission spectra of Au_{25}@BSA excited at 405 nm (Fig. 5b) shows its typical large Stokes-shifted band centred at 660 nm which is the result of a HOMO-LUMO transition followed by an internal intersystem crossing from the initially excited singlet state to a lower-lying triplet state [41].

Meanwhile, the steady state emission spectra of MOF-808/Au_{25}@BSA powders dispersed in water and in solid state excited at the same excitation wavelength (405 nm) result in an emission band which is very similar to the one of bare Au_{25}@BSA, but with a remarkable red shift of about 10 nm (Fig. 6). Similar redshifts are usually caused by changes in the environment that surrounds gold clusters. For example, Raut et al. [40] reported a solvatochromic effect when solvent of Au_{25}@BSA is changed. Moreover, as already observed by Ficarra et al.

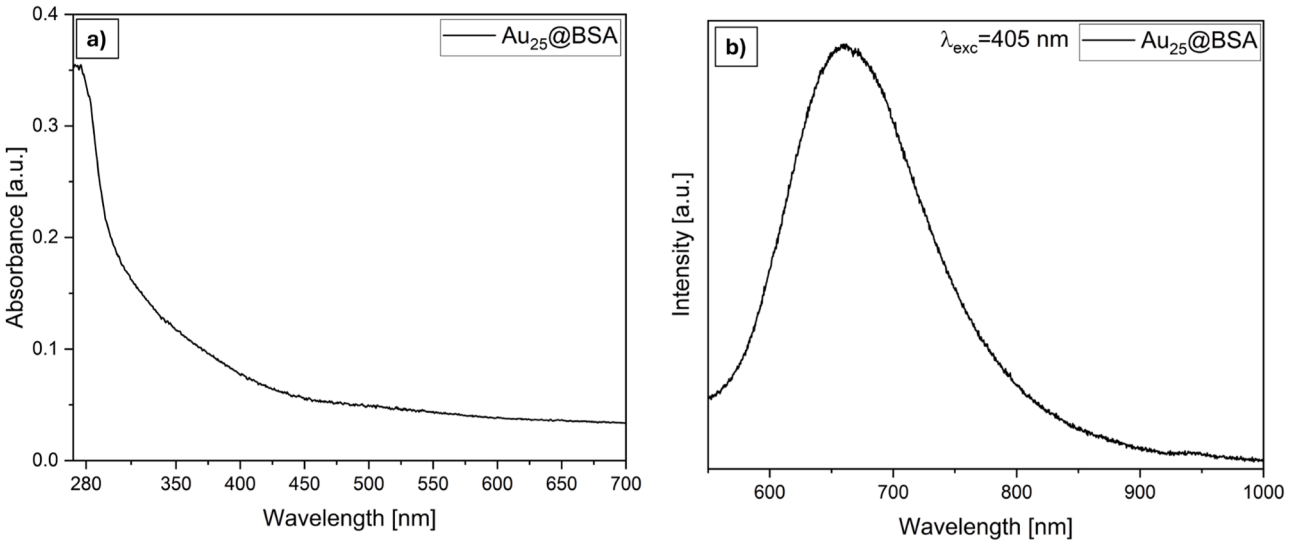

Fig. 5. Absorption (a) and steady state emission spectra (b) of Au_{25}@BSA in water solution.

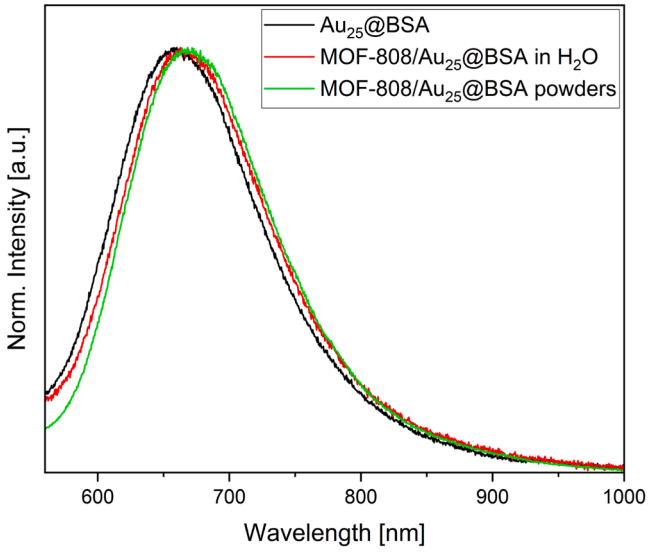

Fig. 6. Steady state emission spectra excited at 405 nm of Au_{25}@BSA in water (black), MOF-808/Au_{25}@BSA powders in water (red) and MOF-808/Au_{25}@BSA powders in solid state (green).

[42], the red shift in the emission band of a luminescent guest species combined with MOF is likely due to electrostatic interactions between the MOF and the luminescent guest. This result is particularly interesting as it represents a spectroscopical evidence of the efficient Au_{25}@BSA loading onto MOF-808. In order to deeply investigate these interactions, we have also performed time resolved photoluminescence (TRPL) to check if the host framework affects the radiative and non-radiative relaxation processes of the gold nanocluster. In Fig. 7 the luminescence decay curves of Au_{25}@BSA and MOF-808/Au_{25}@BSA (λ_{exc}=405 nm) with their respective fits superimposed are reported.

The luminescence of Au_{25}@BSA (Fig. 7**a**) follows a double exponential decay with characteristics lifetimes τ_1= 75 ± 6 ns and τ_2=1.3 ± 0.06 μs which is in good accordance with lifetimes previously reported in literature [37,40,41,43]. While the luminescence of MOF-808/Au_{25}@BSA (Fig. 7**b**) maintains the double exponential decay behaviour, the characteristic lifetimes are sensibly reduced to τ_1= 15 ± 1 ns and τ_2= 330 ± 18 ns. This result could likely be explained by assuming that when Au_{25}@BSA are incorporate in MOF-808 new non radiative channels are activated resulting in an increase of the non-radiative decay component of the overall relaxation process, which is a situation already reported in many cases of incorporation of luminescent guests into MOFs [44]. Therefore, the electrostatic interaction between MOF-808 and Au_{25}@BSA has been confirmed by both steady state and time resolved photoluminescence. Finally, we checked if this interaction could influence the stability on the A_{25}@BSA clusters embedded in MOF structure, by monitoring the steady state emission of the same sample in powders (λ_{exc}= 405 nm) of MOF-808/Au_{25}@BSA during months, as shown in Fig. 8. The emission peak consistently appears around 670 nm, with no significant changes in either intensity or spectral position throughout time. This stability in the emission profile demonstrates the remarkable stability of MOF-808/Au_{25}@BSA and indicates that the photoluminescent properties of Au_{25}@BSA clusters are effectively preserved within the MOF-808 framework. The ability to maintain stable emission over extended periods reinforces the suitability of MOF-808/Au_{25}@BSA as a robust platform for luminescent sensor technologies and offers a considerable improvement over Au_{25}@BSA which have been reported to be not very stable at room temperature and therefore are usually stored at 4 °C [25–27,30]. Indeed, as previously reported by Yuan et al. [45] UV–Vis absorption bands of AuNCs significantly reduce their intensity during the time when they are incubated at 25 °C due to aggregation or structure decomposition of AuNCs thus limiting their practical use.

Furthermore, we investigated the effect of pH and the ionic strength on the luminescence intensity of MOF-808/Au_{25}@BSA dispersed in aqueous solution to evaluate the resilience of the material under varying environmental conditions.

The results, shown in Fig. 9a, indicate that the luminescence remains stable in the pH range of 6–9, with the highest intensity observed at pH 7. A noticeable reduction in luminescence occurs at pH values below 5 and above 9, consistent with previous reports for Au_{25}@BSA clusters alone. This behaviour is attributed to conformational changes in BSA and aggregation of the clusters. However, in MOF-808/Au_{25}@BSA, the luminescence reduction is significantly less pronounced. At pH 2, the luminescence decreases by only 26 % compared to a 50 % reduction observed for Au_{25}@BSA clusters alone [46]. Since drinkable water typically has a pH range of 6.5–8.5 and mercury precipitates as $Hg(OH)_2$ at pH levels above 9, MOF-808/Au_{25}@BSA exhibits strong performance within the optimal pH range for mercury detection [47,48]. Moreover, the relative emission intensity of MOF-808/Au_{25}@BSA remains nearly stable upon varying the ionic strength of KCl solutions, even at concentrations close to that of seawater (0.5 M) highlighting its robustness

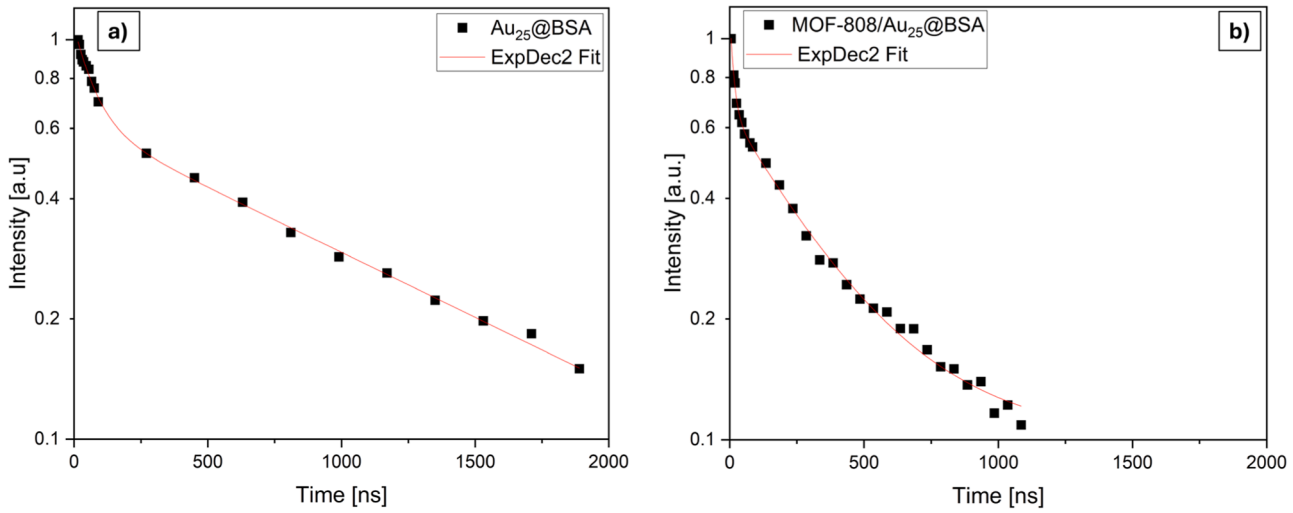

Fig. 7. Luminescence decay curves and respective fits of Au_{25}@BSA in water solution (a) and MOF-808/Au_{25}@BSA powders (b) exited ad 405 nm.

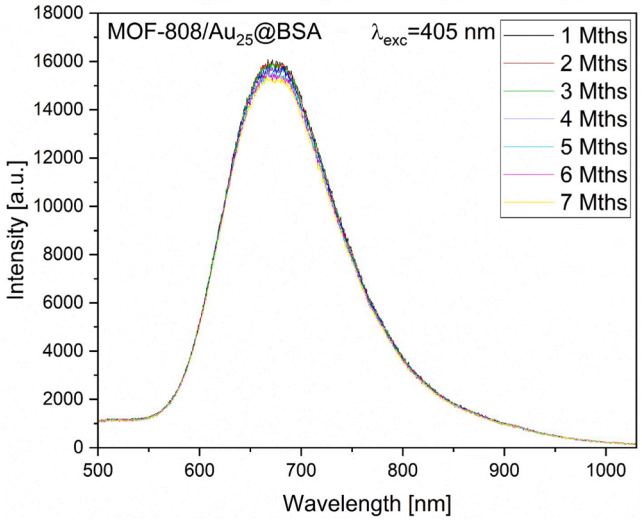

Fig. 8. Steady state emission spectra of MOF-808/Au_{25}@BSA collected during a time span of several months, proving the stability of the composite.

in real-world condition [49].

3.3. Sensing performance

Finally following the structural and optical characterization, the sensing capabilities of MOF-808/Au_{25}@BSA were investigated**.** The sensing performance of MOF-808/Au_{25}@BSA was first evaluated by investigating their response and selectivity to various common metal ions in aqueous solution at a fixed concentration (30 μM). The results are reported in the histogram in Fig. 10.

The histogram in Fig. 10a shows that, under equal concentration conditions, aqueous Hg^{2+} ions selectively quench the luminescence of MOF-808/Au_{25}@BSA powders dispersed in water, resulting in a reduction of the relative emission intensity by approximately 60 %, while other metal ions do not significantly affect the luminescence of this material. Furthermore, the histogram in Fig. 10b compares the luminescence behaviour when Hg^{2+} ions are mixed with other metal ions. The results show that the presence of competing ions does not alter the quenching effect induced by Hg^{2+}. These results confirm the robustness and specificity of the MOF-808/Au_{25}@BSA system for detecting Hg^{2+} in complex aqueous environments. Ours results are consistent with the data reported in the literature for Au_{25}@BSA alone, where Hg^{2+} quenches the luminescence of the AuNCs due to metallophilic Hg–Au(I) interactions. Theoretical studies suggest that dispersion forces between closed-shell metal atoms are highly specific and strong. These interactions are significantly enhanced by relativistic effects, especially in systems involving heavy ions such as Hg^{2+} ($4f^{14}5d^{10}$) and Au^{+} ($4f^{14}5d^{10}$) [26]. Through these non-covalent d^{10}-d^{10} interactions, Hg^{2+} binds to Au^{+} atoms present in the Au_{25}@BSA clusters. Upon binding, Hg^{2+} is reduced to Hg^{+}, forming an Hg-Au amalgam [50]. Furthermore, as reported by Yu et al. [51], Hg^{+} depletes electrons from the excited triplet state of Au_{25}@BSA clusters through efficient electron transfer, leading to luminescence quenching.

These results demonstrate that the sensing properties of Au_{25}@BSA towards Hg^{2+} are retained after incorporation into MOF-808, confirming that MOF-808/Au_{25}@BSA is a promising candidate for detecting Hg^{2+} ions at trace concentrations. Having demonstrated the high selectivity of MOF-808/Au_{25}@BSA towards Hg^{2+} ions, the sensitivity of the material was further investigated through fluorescence titration experiments (Fig. 11a) dispersing the powders in aqueous solution.

Luminescence measurements were conducted by progressively increasing the concentration of Hg^{2+} ions in aqueous solution, ranging from 5.0 to 2000 nM. As observed in the selectivity tests, the luminescence intensity of MOF-808/Au_{25}@BSA, excited at 405 nm, systematically decreased with increasing Hg^{2+} concentration, confirming the quenching effect of Hg^{2+}. From these data, a Stern-Volmer curve was generated by plotting the relative emission intensity against Hg^{2+} concentration, revealing a clear linear relationship in the range of 5–150 nM, with a R^2 value of 0.986 (Fig. 11b). The limit of detection (LOD), calculated as the minimum concentration of quencher that causes a reduction larger than three times the standard deviation of the blank, was 4.6 nM. This is an impressive result given that our LOD is significantly lower– by a factor of two and six – than the U.S. Environmental Protection Agency (USEPA) and World Health Organizzation (WHO) limits for Hg^{2+} in drinking water, which are 9.6 nM (2 ppb) and 29 nM (6 ppb), respectively [52,53]. These results underscore the sensitivity of MOF-808/Au_{25}@BSA as a luminescent sensor for detecting Hg^{2+} at trace levels, complementing the high selectivity observed earlier.

Based on the results reported by Yu et al. and Hu et al., the binding of Hg^{2+} to Au_{25}@BSA does not alter the nanoclusters' luminescence lifetime, indicating that the quenching mechanism follows static quenching [51,54]. Under these conditions, the Stern-Volmer constant K_{SV} in the well-known equation:

$$\frac{I_0}{I} = K_{SV}[Hg^{2+}] + 1$$

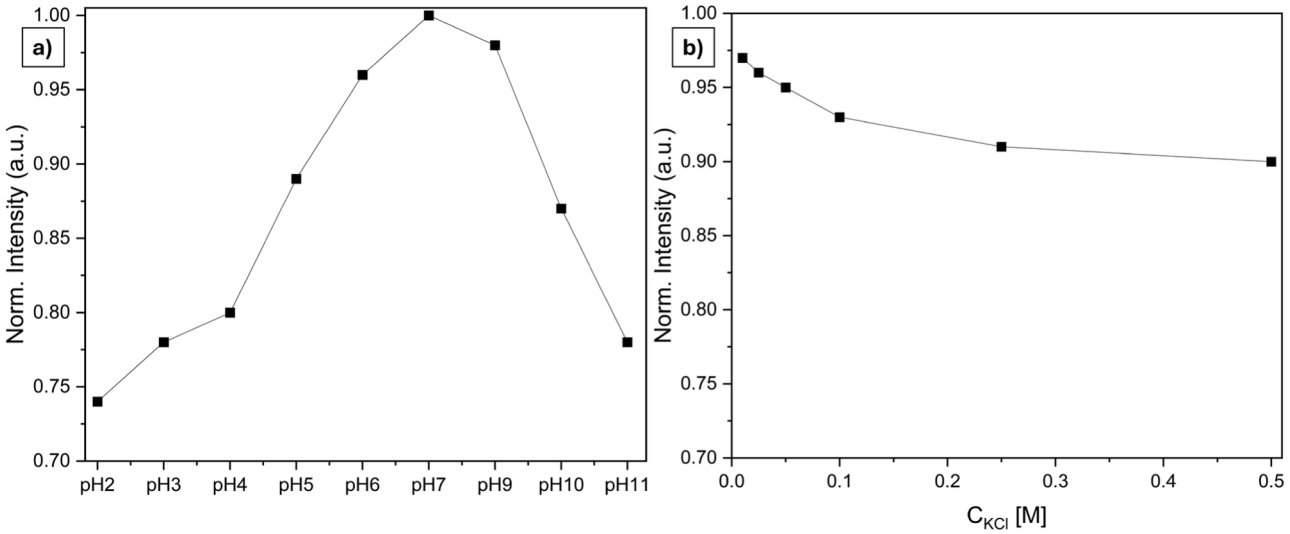

Fig. 9. Normalized luminescence intensity of MOF-808/Au_{25}@BSA dispersed in aqueous solution across different pH values (a) and KCl solutions with different ionic strengths (b).

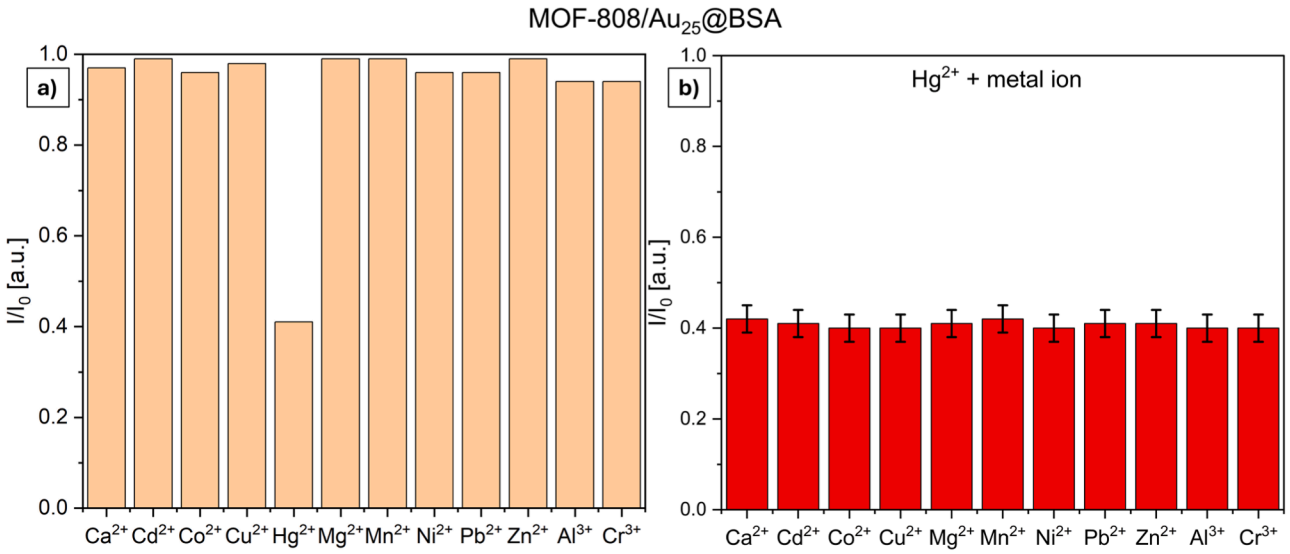

Fig. 10. a) Relative luminescence response of MOF-808/Au_{25}@BSA powders in the presence of various metal ions (30 μM), highlighting strong and selective quenching in the presence of Hg^{2+}. b) Relative luminescence intensity of MOF-808/Au_{25}@BSA in the presence of Hg^{2+} mixed with other metal ions.

is equivalent to the binding constant K_B of the Au_{25}@BSA-Hg^{2+} complex [55]. Accordingly, as reported in Fig. 11b, the binding constant is $K_B=5.91\cdot10^6\ M^{-1}$ ($pK_B=6.77$).

Lastly, we confronted the performance of our MOF-808/Au_{25}@BSA sensor with other novel LMOFs based sensor for Hg^{2+} as reported in Table 1.

The LOD achieved by our sensor (4.6 nM) demonstrates excellent sensitivity, positioning it among the most efficient LMOF-based sensors for Hg^{2+} detection therefore once again demonstrating the worthiness of MOF-808/Au_{25}@BSA as a sensor for Hg^{2+} in aqueous solution.

4. Conclusions

In this study, we successfully developed a highly sensitive and selective luminescent sensor based on MOF-808 embedded with Au_{25}@BSA gold nanoclusters for the detection of Hg^{2+} ions in aqueous environments. The incorporation of Au_{25}@BSA into the MOF-808 framework not only enhanced the thermal and temporal stability of the nanoclusters but also preserved their luminescent properties. Structural characterization confirmed that the MOF-808 maintained its crystalline integrity after loading with Au_{25}@BSA, while optical studies revealed a red-shift in the emission spectrum of the MOF-808/Au_{25}@BSA composite respect to Au_{25}@BSA alone, further supporting the efficient embedding of the nanoclusters. The sensor demonstrated excellent selectivity towards Hg^{2+}, with minimal interference from other common metal ions. Titration experiments showed a clear linear relationship between luminescence quenching and Hg^{2+} concentration in the range of 5–150 nM, with a remarkable detection limit of 4.6 nM. This is significantly below the WHO and USEPA guidelines for mercury in drinking water. These results confirm that the MOF-808/Au_{25}@BSA composite represents a highly effective luminescent sensor for detecting trace levels of Hg^{2+} in aqueous environments. The combination of high selectivity, sensitivity, and long-term stability at room temperature makes this sensor a promising and robust material for environmental monitoring.

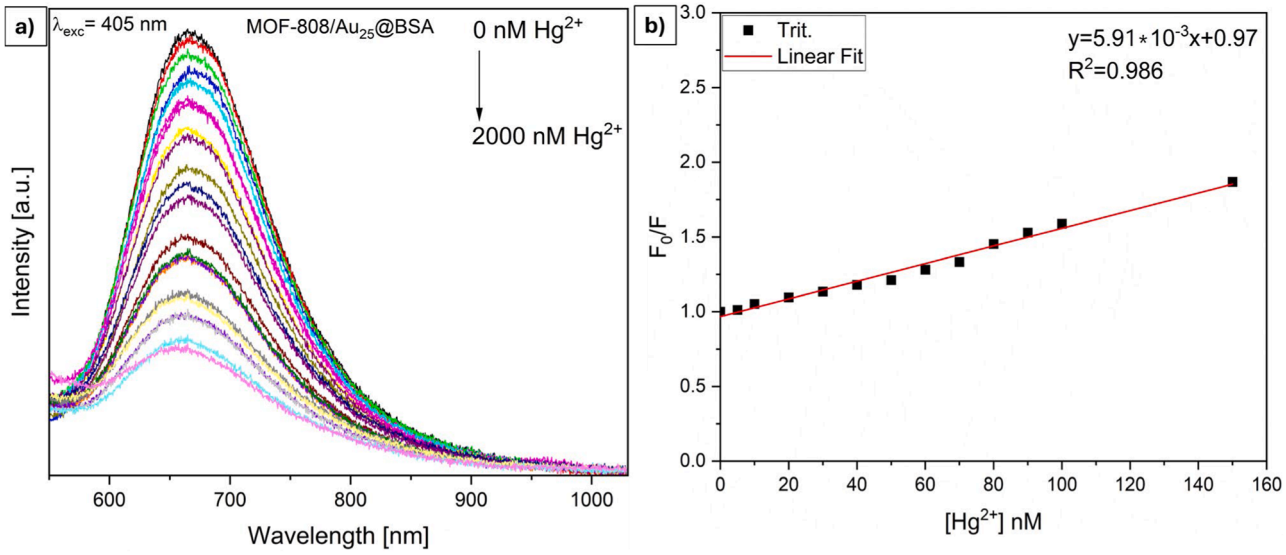

Fig. 11. Titration curve (a) of MOF-808/Au_{25}@BSA with increasing concentrations of Hg^{2+} in aqueous solution, and related calibration curve showing the linear response range of the sensor.

Table 1
Detection performance of different novel LMOFs based sensor for Hg^{2+} compared with MOF-808/Au_{25}@BSA.

LMOFs Sensor	LOD	Ref.
$[Pb_2(2\text{-NCP})_2(NH_2\text{-BDC})]_n$	6.48 μM	[56]
Cd-L-NDA MOF	351 nM	[57]
Ba-Eu-MOF	220 nM	[58]
2HA = N-UiO-66(Zr)	202.4 nM	[59]
$Mn_3(C_{10}H_4O_7N_1)_2(8H_2O)]\cdot H_2O$	177 nM	[60]
2D Eu_xCe_{1-x}-bop NSs	167 nM	[61]
NH_2_MIL-53(Al)	150 nM	[21]
5Br_2HA = N-Al-MOF	82.3 nM	[62]
$Cd_3(C_{10}H_4O_7N_1)_2(8H_2O)]\cdot H_2O$	16.7 nM	[60]
UiO-66@Butyne	10.9 nM	[63]
PCN-221	10 nM	[64]
Eu^{3+}@UiO-66(DPA)	8.26 nM	[65]
TbTATAB	4.4nM	[66]
NXS@ZIF-8	4.39 nM	[67]
Eu-Ca-MOF	2.6 nM	[22]
NH_2-UiO-66/g-CNQDs	2.4 nM	[68]
$[La_3(NDC)_4(DMF)_3(H_2O)_4]_n$	2.0 nM	[69]
$\{[Eu_2(L)(phen)_2(ox)_2(H_2O)_2]\cdot 10H_2O\cdot phen\}_n$	1.5 nM	[70]
NIIC-3-Tb	0.88 nM	[71]
MOF-808/Au_{25}@BSA	4.6 nM	This work

CRediT authorship contribution statement

L.G. Barbata: Writing – review & editing, Writing – original draft, Investigation, Formal analysis, Data curation. **M. Mazaj:** Writing – review & editing, Supervision, Resources, Investigation, Formal analysis. **R. Ettlinger:** Writing – review & editing, Supervision, Investigation, Formal analysis. **G. Ficarra:** Writing – review & editing, Visualization, Investigation, Formal analysis, Data curation. **P. Castronovo:** Writing – review & editing, Investigation, Data curation. **A. Sciortino:** Writing – review & editing, Supervision, Data curation. **F. Messina:** Writing – review & editing, Supervision. **R.E. Morris:** Writing – review & editing, Supervision, Resources, Conceptualization. **G. Buscarino:** Writing – review & editing, Supervision, Resources.

Declaration of competing interest

The authors declare that they have no known competing financial interests or personal relationships that could have appeared to influence the work reported in this paper.

Acknowledgments

We acknowledge Slovenian Research and Innovation Agency for financing (program number P1–0021).

Supplementary materials

Supplementary material associated with this article can be found, in the online version, at doi:10.1016/j.materresbull.2025.113397.

Data availability

Data will be made available on request.

References

[1] C. Janiak, J.K. Vieth, New J. Chem. 34 (11) (2010) 2366, https://doi.org/10.1039/C0NJ00275E.
[2] H. Furukawa, et al., Science 341 (6149) (2013) 1230444, https://doi.org/10.1126/science.1230444.
[3] T. Jia, et al., J. Environ. Chem. Eng. 10 (5) (2022) 108300, https://doi.org/10.1016/j.jece.2022.108300.
[4] H. Li, et al., Mater. Today 2 (21) (2018) 108–121, https://doi.org/10.1016/j.mattod.2017.07.006.
[5] A.I. Osman, et al., Environ. Chem. Lett. 19 (2021) 797–849, https://doi.org/10.1007/s10311-020-01133-3.
[6] T. Ghanbari, et al., Sci. Total Environ. 707 (2020) 135090, https://doi.org/10.1016/j.scitotenv.2019.135090.
[7] A. Bavykina, et al., Chem. Rev. 120 (16) (2020) 8468–8535, https://doi.org/10.1021/acs.chemrev.9b00685.
[8] A. Dhakshinamoorthy, et al., Chem. Soc. Rev. 47 (2018) 8134–8172, https://doi.org/10.1039/C8CS00256H.
[9] Y. Sun, et al., Nano-Micro Lett. 12 (1) (2020) 103, https://doi.org/10.1007/s40820-020-00423-3.
[10] H.D. Lawson, et al., ACS Appl. Mater. Interf. 13 (6) (2021) 7004–7020, https://doi.org/10.1021/acsami.1c01089.
[11] Y. Zhang, et al., Coord. Chem. Rev. 354 (2018) 28–45, https://doi.org/10.1016/j.ccr.2017.06.007.
[12] M. Allendorf, et al., Chem. Soc. Rev. 38 (5) (2009) 1330–1352, https://doi.org/10.1039/b802352m.
[13] Y. Cui, et al., Chem. Rev. 112 (2) (2012) 1126–1162, https://doi.org/10.1021/cr200101d.
[14] Y. Zhang, et al., Coord. Chem. Rev. 354 (2018) 28–45, https://doi.org/10.1016/j.ccr.2017.06.007.
[15] L.E. Kreno, et al., Chem. Rev. 112 (2) (2012) 1105–1125, https://doi.org/10.1021/cr200324t.
[16] J.-D. Park, et al., J. Prevent. Med. Public Health 45 (6) (2012) 344–352, https://doi.org/10.3961/jpmph.2012.45.6.344.
[17] J.F. Callan, et al., Tetrahedron 61 (36) (2005) 8551–8588, https://doi.org/10.1016/j.tet.2005.05.043.

[18] S.P. Kollur, et al., Separations 8 (10) (2021) 192, https://doi.org/10.3390/separations8100192.
[19] H. Alzaimoor, et al., Crit. Rev. Analyt. Chem. (2023) 1–22, https://doi.org/10.1080/10408347.2023.2220800.
[20] Z.L. Magnuson, et al., 3 - Sensing and Sequestration of Inorganic Cationic Pollutants By Metal-Organic frameworks, in Metal-Organic Frameworks (MOFs) For Environmental Applications Ed.(s): Sujit K. Ghosh, Elsevier, 2019, pp. 63–93, https://doi.org/10.1016/B978-0-12-814633-0.00005-3. PagesISBN 9780128146330.
[21] L. Zhang et al. *Inorg. Chem.* 58 (19), 12573–12581. https://doi.org/10.1021/acs.inorgchem.9b01242.
[22] N.W.H. Guo, et al., Talanta 250 (2022) 123710, https://doi.org/10.1016/j.talanta.2022.123710.
[23] R. Jin, et al., Chem. Rev. 116 (18) (2016) 10346–10413, https://doi.org/10.1021/acs.chemrev.5b00703.
[24] R. Jin, Nanoscale 2 (3) (2010) 343–362, https://doi.org/10.1039/b9nr00160c.
[25] J. Xie, et al., J. Am. Chem. Soc. 131 (3) (2009) 888–889, https://doi.org/10.1021/ja806804u.
[26] J. Xie, et al., Chem. Commun. 46 (6) (2010) 961–963, https://doi.org/10.1039/b920748a.
[27] X. Kang, Nanoscale 10 (2018) 10758–10834, https://doi.org/10.1039/C8NR02973C.
[28] H. Furukawa, et al., J. Am. Chem. Soc. 136 (11) (2014) 4369–4381, https://doi.org/10.1021/ja500330a.
[29] S. Dai, et al., Chem. Mater. 33 (17) (2021) 7057–7066, https://doi.org/10.1021/acs.chemmater.1c02174.
[30] G. Guan, et al., Chem. Commun. 50 (43) (2014) 5703–5705, https://doi.org/10.1039/C4CC02008A.
[31] J. Rouquerol, P. Llewellyn and F. Rouquerol, in P. L. Llewellyn, F. Rodriquez-Reinoso, J. Rouqerol and N. Seaton (Eds.), Characterization of Porous Solids VII, Elsevier, 2007, vol. 160, pp. 49–56. ISBN: 9780444520227.
[32] S. Krista, et al., J. Am. Chem. Soc. 129 (27) (2007) 8552–8556, https://doi.org/10.1021/ja071174k.
[33] D. Cao, et al., Biosen. Bioelect. 42 (2013) 47–50, https://doi.org/10.1016/j.bios.2012.10.084.
[34] Y. Zhang, et al., Sen. Actuat. B: Chem. 235 (2016) 386–393, https://doi.org/10.1016/j.snb.2016.05.108.
[35] G. Zhang, Sen. Actuat. B: Chem. 183 (2013) 583–588, https://doi.org/10.1016/j.snb.2013.04.023.
[36] I. Romero-Muñiz, et al., ACS Appl. Mater. Interf. 14 (23) (2022) 27040–27047, https://doi.org/10.1021/acsami.2c04712.
[37] A. Retnakumari, et al., Nanotechnology 21 (5) (2010) 055103, https://doi.org/10.1088/0957-4484/21/5/055103.
[38] K. Xuan, et al., Chin. J. Cataly. 40 (4) (2019) 553–566, https://doi.org/10.1016/S1872-2067(19)63291-2.
[39] G. Zschornack, Handbook of X-Ray Data, Springer Berlin ISBN: 9783540286196 https://doi.org/10.1007/978-3-540-28619-6.
[40] S. Raut, et al., Nanoscale 5 (8) (2013) 3441–3446, https://doi.org/10.1039/c3nr34152f.
[41] X. Wen, et al., J. Phys. Chem. C 116 (35) (2012) 19032–19038, https://doi.org/10.1021/jp305902w.
[42] G. Ficarra, et al., Phys. Chem. Chem. Phys. 26 (33) (2024) 22269–22277, https://doi.org/10.1039/D4CP02279C.
[43] S. Chandra, et al., Adv. Optical Mater. 11 (2023) 2202649, https://doi.org/10.1002/adom.202202649.
[44] M. Gutiérrez, et al., Chem. Rev. 122 (11) (2022) 10438–10483, https://doi.org/10.1021/acs.chemrev.1c00980.
[45] X. Yuan, et al., Nano Res. 8 (2015) 3488–3495, https://doi.org/10.1007/s12274-015-0847-2.
[46] X.L. Cao, et al., Vib. Spectrosc. 65 (2013) 186–192, https://doi.org/10.1016/j.vibspec.2013.01.004.
[47] B.M. Saalidong, et al., PLoS One 17 (1) (2022) e0262117, https://doi.org/10.1371/journal.pone.0262117.
[48] M. Ugrina, et al., Processes 8 (11) (2020) 1523, https://doi.org/10.3390/pr8111523.
[49] F.J. Millero, Pure appl. chem. 57 (8) (1985) 1015–1024, https://doi.org/10.1351/pac198557081015.
[50] A. Senthamizhan, et al., Sci. Rep. 5 (2015) 10403, https://doi.org/10.1038/srep10403.
[51] P. Yu, et al., Part Part Syst. Charact. 30 (5) (2013) 467–472, https://doi.org/10.1002/ppsc.201200111.
[52] USEPA (2009) National Primary Drinking Water Regulations. United States Environmental Protection Agency EPA 816-F-09-004, May 2009. https://nepis.epa.gov/Exe/ZyPURL.cgi?Dockey=P1005EJT.txt.
[53] Guidelines For Drinking-Water Quality: Fourth Edition Incorporating the First and Second Addenda, World Health Organization, Geneva, 2017. ISBN: 978-92-4-004506-4, https://www.who.int/publications/i/item/9789240045064.
[54] D. Hu, et al., Analyst 135 (2010) 1411–1416, https://doi.org/10.1039/C000589D.
[55] J.R. Lakowicz, Principles of Fluorescence Spectroscopy, 3rd edition, Springer, New York, 2006, https://doi.org/10.1007/978-0-387-46312-4. ISBN: 9780387463124.
[56] Y. Qiao, et al., J. Solid State Chem. 290 (2020) 121610, https://doi.org/10.1016/j.jssc.2020.121610.
[57] J. Zhang, et al., Inorg. Chem. 64 (1) (2025), https://doi.org/10.1021/acs.inorgchem.4c04672, 335-34.
[58] H. Wang, et al., Anal. Chem. 92 (4) (2020) 3366–3372, https://doi.org/10.1021/acs.analchem.9b05410.
[59] M.A. El-Bindary, et al., Appl. Organomet. Chem. 37 (5) (2023) e7070, https://doi.org/10.1002/aoc.7070.
[60] K. Manna, S. Natarajan, Inorg. Chem. 62 (1) (2023) 508–519, https://doi.org/10.1021/acs.inorgchem.2c03679.
[61] Y. Li, et al., Talanta 278 (2024) 126456, https://doi.org/10.1016/j.talanta.2024.126456.
[62] M.A. Khalil, et al., Appl. Organomet Chem. 38 (8) (2024) e7571, https://doi.org/10.1002/aoc.7571.
[63] P. Samanta, et al., Inorg. Chem. 57 (5) (2018) 2360–2364, https://doi.org/10.1021/acs.inorgchem.7b02426.
[64] E. Moradi, et al., J. Solid State Chem. 286 (2020) 121277, https://doi.org/10.1016/j.jssc.2020.121277.
[65] Z. Xiaoxiong, et al., Inorg. Chem. 58 (6) (2019) 3910–3915, https://doi.org/10.1021/acs.inorgchem.8b03555.
[66] T. Xia, et al., Chem. Eur. J. 22 (51) (2016) 18429, https://doi.org/10.1002/chem.201603531.
[67] N. Gao, et al., Talanta 286 (2025) 127553, https://doi.org/10.1016/j.talanta.2025.127553.
[68] K. Sonowal, L. Saikia, J. Environ. Sci. 126 (2023) 531–544, https://doi.org/10.1016/j.jes.2022.05.032.
[69] S. Geranmayeh, et al., J. *Fluoresc* 33 (2023) 1017–1026, https://doi.org/10.1007/s10895-022-03124-9.
[70] L. Fan, et al., Microchem. J. 196 (2024) 109712, https://doi.org/10.1016/j.microc.2023.109712.
[71] X. Yu, et al., Angew. Chem. Int. Ed. 63 (2024) e202410509, https://doi.org/10.1002/anie.202410509.